



Efficient photothermal catalytic oxidation of toluene by $\text{La}_{1-x}\text{Fe}_x\text{MnO}_3$ with full spectrum response: The effects of Fe doping and photoactivation

Qi Yu^{a,b}, Caiting Li^{a,b,*}, Jungang Zhao^{a,b}, Xuan Liu^{a,b}, Le Huang^{a,b}, Youcai Zhu^{a,b}, Kuang Yang^{a,b}, Ziang Zhang^{a,b}, Dengsheng Ma^{a,b}, Ying Zhang^{a,b}, Qi Huang^{a,b}

^a College of Environmental Science and Engineering, Hunan University, Changsha 410082, PR China

^b Key Laboratory of Environmental Biology and Pollution Control (Hunan University), Ministry of Education, Changsha 410082, PR China

ARTICLE INFO

Keywords:

Photothermal catalysis
Fe doping
Photoactivation
Reactive oxygen species
Toluene oxidation

ABSTRACT

Developing efficient photothermal catalysts with full spectrum response is one of the frontier topics in photothermal catalytic of VOCs. In this work, $\text{La}_{1-x}\text{Fe}_x\text{MnO}_3$ ($0 \leq x \leq 0.2$) was synthesized via citrate sol-gel method. Under full spectrum illumination of $1.3 \times 10^4 \text{ W/m}^2$, $\text{La}_{0.9}\text{Fe}_{0.1}\text{MnO}_3$ exhibited a more superior activity (86.7% toluene conversion and 84.6% CO_2 yield). Through controlled experiments, not only the origin of photothermal activity, but the possible intrinsic drivers (Fe doping and photoactivation) of the enhanced activity were also revealed. Particularly, the mechanistic details of their facilitating reactions were thoroughly studied, where the improved mobility and activation of lattice oxygen played the primary role. Moreover, the co-effect of Fe doping and photoactivation on the resistance to complex gas components (SO_2 , H_2O) and durability was systematically investigated. Eventually, the plausible pathways and mechanisms of toluene oxidation were proposed. This study provides a new insight into photothermal catalysts with full spectrum response for environmental remediation.

1. Introduction

In recent years, some hazardous volatile organic compounds (VOCs) have attracted growing attention (e.g., formaldehyde, benzene, toluene, and acetone) due to their carcinogenic and teratogenic properties [1], as well as being important precursors of ozone, particulate matter, and photochemical smog, which adversely affect human health and ecological environment [2]. Many end-of-pipe methods have been applied to eliminate VOCs, such as absorption [3], plasma decomposition [4], and photo/thermal catalytic oxidation [5,6]. At present, photo/thermal catalytic oxidation (PCO/TCO) is the dominant technology to degrade VOCs into harmless products [7,8]. However, PCO is usually limited by the low efficiency of light-utilization, while TCO requires high energy consumption, which hinders their further development [9]. Photothermal catalytic oxidation (PTCO) provides a novel strategy to stimulate the synergy between PCO and TCO, which is currently one of the frontier research topics for VOCs degradation [10,11]. It perfectly combines the high catalytic efficiency and stability of TCO with the low energy consumption of PCO, and with this approach, the ultraviolet (UV), visible (VIS), and infrared (IR) light in solar light can be exploited more effectively [12]. In other words, PTCO provides a more efficient

conversion of solar (especially for low-energy photons) to chemical energy, which is of great significance for solving energy and environmental problems. Moreover, light has been shown to have an activating effect on the surface oxygen species, which can significantly optimize the reaction path [13]. PTCO technology is also found to promote water resistance and coke resistance while simultaneously enhancing catalytic activity [14,15]. Therefore, PTCO is expected to be effective in restraining the deactivation of catalyst, which makes it promising for practical complex flue gas applications, especially in industrial painting, steel plants, and petrochemical industries [5].

Since the majority of the energy required for PTCO reaction is derived from light-to-heat conversion [16], the broad light wavelength absorption (covering IR range) and efficient photothermal conversion (coupling the captured photons into thermal energy) are prerequisites for an ideal photothermal catalyst. Recent studies have confirmed that ABO_3 -type perovskite oxides may be one of the promising photothermal catalyst candidates [17,18]. Thereinto, LaMnO_3 -based materials receive much focus in photothermal catalysis of VOCs due to their great reducibility and surface oxygen availability. As reported by Chen et al. [19], LaMnO_3 showed great catalytic activity for gaseous styrene under VIS illumination, and Li et al. [17] demonstrated that toluene could be

* Corresponding author at: College of Environmental Science and Engineering, Hunan University, Changsha, 410082, PR China.

E-mail address: ctli@hnu.edu.cn (C. Li).

<https://doi.org/10.1016/j.apcatb.2023.122441>

efficiently oxidized on CeO₂/LaMnO₃ under IR illumination. In general, VIS-IR light with low photon energy has a limited ability to excite the traditional PCO, but it exhibits a significant heating effect, thus driving the redox reactions [20]. Additionally, it had been reported that the light in the high-energy UV region could excite photogenerated carriers over LaMnO₃-based materials, and further actuated the PCO reaction [21]. If the high-energy UV region and VIS-IR region are combined to couple the optical and thermal effects, LaMnO₃-based materials will show a more distinctive PTCO performance. Nevertheless, it has not been systematically investigated so far.

On the other hand, the A-site cations in LaMnO₃ perovskites, which are not catalytically active, will preferentially occupy the native surface, resulting in unsatisfactory catalytic performance [22]. Researchers have worked extensively on this issue. It was proposed that the structural modification of perovskites by in situ heteroatom doping into the lattice framework could be a feasible and efficient strategy [23]. For example, the partial substitution of A-site La by some metal cations (e.g., Sr, K, Ce, Co) can regulate the valence state of the B-site active metal, promote rapid electron transfer, and improve the redox properties while maintaining structural stability [24–26]. Fe has also been shown to be a promising dopant for the A/B-site of LaMnO₃, where the doping at B-site could improve the concentration of reactive oxygen species and reducibility in the degradation of o-xylene, and the A-site doping promoted the reactivity and thermal stability in chemical looping reforming of methane [4,27]. However, to the best of our knowledge, few studies are devoted to the role of Fe for the A-site doped LaMnO₃ in VOCs oxidation.

Herein, in this work, a series of Fe doped LaMnO₃ at A-site photo-thermal catalysts (La_{1-x}Fe_xMnO₃, 0 ≤ x ≤ 0.2) were synthesized via sol-gel method, and their physicochemical properties were characterized. Their PTCO performance of toluene was evaluated under full spectrum illumination, and it was further unraveled that the photothermal activity mainly derived from the light-driven heat. The results also showed that Fe doping and photoactivation synergistically promoted the oxidation of toluene. By combining multiple analytical techniques, the mechanistic details of the advanced activity driven by Fe doping and photoactivation were thoroughly studied. The mobility and activation of lattice oxygen species were found to play the primary role. Moreover, we proposed the possible pathways for toluene oxidation, and the co-effect of Fe doping and photoactivation on catalysts resistance and durability was also investigated. It is envisaged that the elucidation of Fe doping and photoactivation effects gives a more explicit direction for developing effective photothermal perovskite catalysts for environmental preservation.

2. Experimental section

2.1. Samples preparation

La_{1-x}Fe_xMnO₃ samples (x = 0, 0.05, 0.10, 0.15, 0.20) were synthesized via citrate sol-gel method. More details can be found in the Text S1 of [Supplementary Information](#).

2.2. Samples characterization

The physicochemical properties of samples were investigated by diverse techniques, including X-ray diffraction (XRD), scanning electron microscopy (SEM), Brunauer-Emmett-Teller (BET), inductively coupled plasma optical emission spectrometry (ICP-OES), X-ray photoelectron spectroscopy (XPS), Fourier transform infrared spectroscopy (FTIR), UV-VIS-IR diffuse reflectance spectroscopy (DRS), electron paramagnetic resonance (EPR), temperature-programmed desorption of O₂ (O₂-TPD), temperature-programmed reduction of H₂ (H₂-TPR), temperature-programmed reduction of CO (CO-TPR), in situ diffuse reflectance infrared Fourier transform spectroscopy (in situ DRIFTS),

and ¹⁸O₂ isotope tracing experiment. The detailed characterization methods were described in the Text S2.

2.3. Calculation method

Density functional theory (DFT) calculations were conducted by Vienna Ab initio Simulation Package (VASP, version 6.2.1). The perovskite structure Fe doped LaMnO₃ models (La_{0.9}Fe_{0.1}MnO₃) were generated based on the (110) surface of standard perovskite structure (Pm-3 m (221)) LaMnO₃ system (Fe: La=1: 9), and selected the optimal one (constructure II) from three different constructions ([Fig. S1](#)), the optimized structure of LaMnO₃ and La_{0.9}Fe_{0.1}MnO₃ were also presented. More details on the calculations were provided in Text S3.

2.4. Catalytic performance evaluation

2.4.1. Photothermal catalytic activity

As shown in [Fig. S2](#), the photothermal catalytic performance of La_{1-x}Fe_xMnO₃ (0 ≤ x ≤ 0.2) for toluene was evaluated in a cylindrical stainless-steel reactor with a quartz window under a 300 W Xe lamp (PLS-SXE300+, λ= 320–2500 nm). The light intensity was adjusted between 0.7 and 1.3 × 10⁴ W/m² (corresponding 7–13 SUN intensity). The 0.1 g catalyst was later coated on the sand core with a diameter of 80 mm, and the surface temperature was measured by locating a thermocouple on the center of the catalyst layer. The simulated air flow (20% O₂/N₂) carrying 500 ppm toluene was passed through the catalyst layer at a total flow rate of 50 mL/min, giving a gas hourly space velocity (GHSV) of 30,000 mL/(g·h). In the case of water vapor introduction, 3–15 vol% H₂O was introduced by passing the feed stream through a water saturator at a certain temperature. For introducing SO₂, 100 ppm SO₂ from a 2000 ppm SO₂ cylinder (balanced with N₂) was introduced to the reaction system via a mass flow controller.

Prior to illumination, the sample was pretreated under simulated air flow at room temperature for 1 h, enabling adsorption-desorption equilibrium of toluene on the catalyst layer. The concentration of toluene was monitored by an online gas chromatograph (GC, GC-2014C, SHIMADZU) equipped with a flame ionization detector (FID), and CO₂ as the final product was detected by PGA-650 (Phymetrix, USA). The toluene conversion and CO₂ yield were calculated by [Eqs. \(1\) and \(2\)](#), respectively. The standard deviations were calculated from the repeated measurements of catalytic performance curves, and the standard deviations were all below 3%.

Additionally, the turnover frequencies (TOF, S⁻¹) values, Fe content and surface area normalized reaction rates (r_{Fe}^* , mol·g_{Fe}⁻¹·s⁻¹, $r_{S_{BET}}^*$, mol·m⁻²·s⁻¹) were calculated in Text S4.

$$\text{Toluene conversion (\%)} = \frac{[\text{Toluene}]_{\text{in}} - [\text{Toluene}]_{\text{out}}}{[\text{Toluene}]_{\text{in}}} \times 100\% \quad (1)$$

$$\text{CO}_2 \text{ yield (\%)} = \frac{[\text{CO}_2]_{\text{produced}}}{[\text{CO}_2]_{\text{theoretical}}} \times 100\% \quad (2)$$

Where [Toluene]_{in} and [Toluene]_{out} represent the inlet and outlet concentration of toluene, respectively; [CO₂]_{produced} and [CO₂]_{theoretical} are the concentration of CO₂ produced in outlet gas and the theoretical value for complete conversion of toluene, respectively.

2.4.2. Thermocatalytic activity

The thermocatalytic oxidation (TCO) activity of the samples for toluene was evaluated on a tubular quartz reactor (i.d.= 6.00 mm, length= 600 mm) at different temperatures. The catalyst dosage, toluene concentration, gas component, and flow rate were consistent with the PTCO conditions. The experimental procedure was detailed in our previous publication [28].

3. Results and discussion

3.1. Catalytic performance

The PTCO performance of $\text{La}_{1-x}\text{Fe}_x\text{MnO}_3$ ($0 \leq x \leq 0.2$) samples with varied light intensity for gaseous toluene was evaluated under full spectrum (UV–VIS–IR) illumination. As illustrated in Fig. 1a and b, with the elevated light intensity from $0.7, 0.9, 1.1\text{--}1.3 \times 10^4 \text{ W/m}^2$, the toluene conversion and CO_2 yield of all samples increased markedly, and the CO_2 yield displayed a transient and abrupt rise after raising the illumination intensity, which probably due to the decomposition of accumulated intermediates. Obviously, Fe doping improved the catalytic activity and selectivity significantly. After the light illumination of $1.3 \times 10^4 \text{ W/m}^2$ for 90 min, their performance followed the sequence: $\text{La}_{0.9}\text{Fe}_{0.1}\text{MnO}_3 > \text{La}_{0.95}\text{Fe}_{0.05}\text{MnO}_3 > \text{La}_{0.85}\text{Fe}_{0.15}\text{MnO}_3 > \text{La}_{0.8}\text{Fe}_{0.2}\text{MnO}_3 > \text{LaMnO}_3$, where $\text{La}_{0.9}\text{Fe}_{0.1}\text{MnO}_3$ performed the best with maximum toluene conversion of 86.7% and CO_2 yield of 84.6%. Notably, as a control, the commercial TiO_2 (P25) showed quite inert in the PTCO of toluene (Fig. S3). And for comparison with previously reported photothermal catalysts (Table S1), $\text{La}_{0.9}\text{Fe}_{0.1}\text{MnO}_3$ also exhibits remarkable performance. Interestingly, $\text{La}_{0.95}\text{Fe}_{0.05}\text{MnO}_3$ exhibited a greater improvement at lower light intensity of 0.7 and $0.9 \times 10^4 \text{ W/m}^2$, whereas the $\text{La}_{0.85}\text{Fe}_{0.15}\text{MnO}_3$ and $\text{La}_{0.8}\text{Fe}_{0.2}\text{MnO}_3$ improved poorly. This phenomenon indicates that the effect on the catalytic performance varies with the amount of Fe doping. Since La in LaMnO_3 was usually inert species and not involved in the catalytic reaction, while the B-site Mn was catalytically active, we calculated the TOF per unit amount of Mn ions to assess the effect of Fe doping at a conversion less than 20% [17]. The results in Table S2 showed that the $\text{La}_{0.9}\text{Fe}_{0.1}\text{MnO}_3$ exhibited the highest TOF values. Furthermore, by normalizing the toluene reaction rate with Fe weight, their catalytic performance was contrasted with excluding minor differences in Fe doping among samples. As Table S2, $\text{La}_{0.9}\text{Fe}_{0.1}\text{MnO}_3$ also exhibited the highest reaction rate, both normalized by Fe content ($1.03 \times 10^{-5} \text{ mol}\cdot\text{g}_{\text{Fe}}^{-1}\cdot\text{s}^{-1}$) and surface area ($2.96 \times 10^{-7} \text{ mol}\cdot\text{m}^{-2}\cdot\text{s}^{-1}$). Therefore, we suggest that the beneficial interaction between Fe and LaMnO_3 has no linear relationship with the content of Fe doping, and when the appropriate amount of Fe is 0.1, it gives a more desirable performance.

Additionally, the long-term PTCO performance of $\text{La}_{0.9}\text{Fe}_{0.1}\text{MnO}_3$ was tested under the light illumination of $1.3 \times 10^4 \text{ W/m}^2$. As shown in Fig. 1c, the toluene conversion and CO_2 yield only exhibited a slight decrease in a 34 h toluene stream (500 ppm), illustrating outstanding durability. And the stability of $\text{La}_{0.9}\text{Fe}_{0.1}\text{MnO}_3$ was investigated by repeatedly changed the light intensity, the results of Fig. S4 showed the excellent stability of $\text{La}_{0.9}\text{Fe}_{0.1}\text{MnO}_3$. We also conducted the cyclic tests (2 h per cycle) to measure the cyclability of $\text{La}_{0.9}\text{Fe}_{0.1}\text{MnO}_3$. It could be seen from Fig. 1d, after 8 th cycle, the toluene conversion and CO_2 yield were still kept as high as 85.7% and 83.3%, respectively. These are important indicators to evaluate whether the catalyst has potential applicability in the real exhaust, the $\text{La}_{0.9}\text{Fe}_{0.1}\text{MnO}_3$ with excellent durability, stability and cyclability is expected to be a promising photothermal catalyst in practical application.

3.2. Origin of activity

According to the synergistic mode, photothermal catalysis can be classified into thermal-assisted photocatalysis, light-assisted thermal catalysis, and photothermal co-catalysis [12]. To deeply understand the PTCO mechanism over $\text{La}_{1-x}\text{Fe}_x\text{MnO}_3$ ($0 \leq x \leq 0.2$) samples, it is necessary to figure out the origin of activity. Thereby, the optical absorption capacity of all samples (Fig. 2a) was first investigated. The LaMnO_3 exhibited intense absorption between 200 nm and 2500 nm, processing great ability in light utilization, which was consistent with the previous reports [17,19]. After the doping of Fe, the samples maintained a broad and intense absorption. However, it was weakened with the increase of Fe content, especially in the IR region. Generally, the samples with strong absorption in the VIS–IR region enable it a highly active photothermal responsive that absorbs light and releases the absorbed photons as heat efficiently. To further measure the photothermal conversion ability of samples, their equilibrium temperature under light illumination was recorded as Fig. 2b. The sequencing of the equilibrium temperature on these samples corresponded well to the DRS results. Such energy supply from the effective photo-thermal conversion could maintain the surface temperature of samples at about 180°C , thus potentially driving the occurrence of some endothermic reactions, such as the oxidation of toluene.

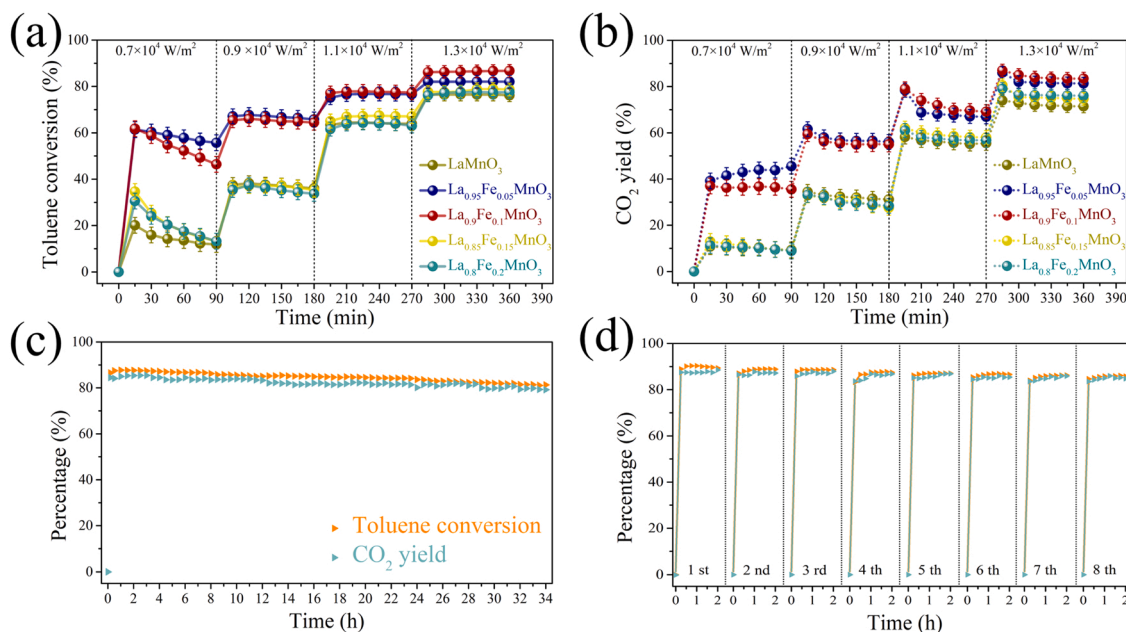


Fig. 1. (a) Toluene conversion and (b) CO_2 yield over $\text{La}_{1-x}\text{Fe}_x\text{MnO}_3$ ($0 \leq x \leq 0.2$) samples with varied light intensity under full spectrum illumination. The durability (c) and cyclability tests (d) of PTCO performance on $\text{La}_{0.9}\text{Fe}_{0.1}\text{MnO}_3$. (Reaction condition: 500 ppm toluene, 20 vol% O_2/N_2 , light intensity= $1.3 \times 10^4 \text{ W/m}^2$).

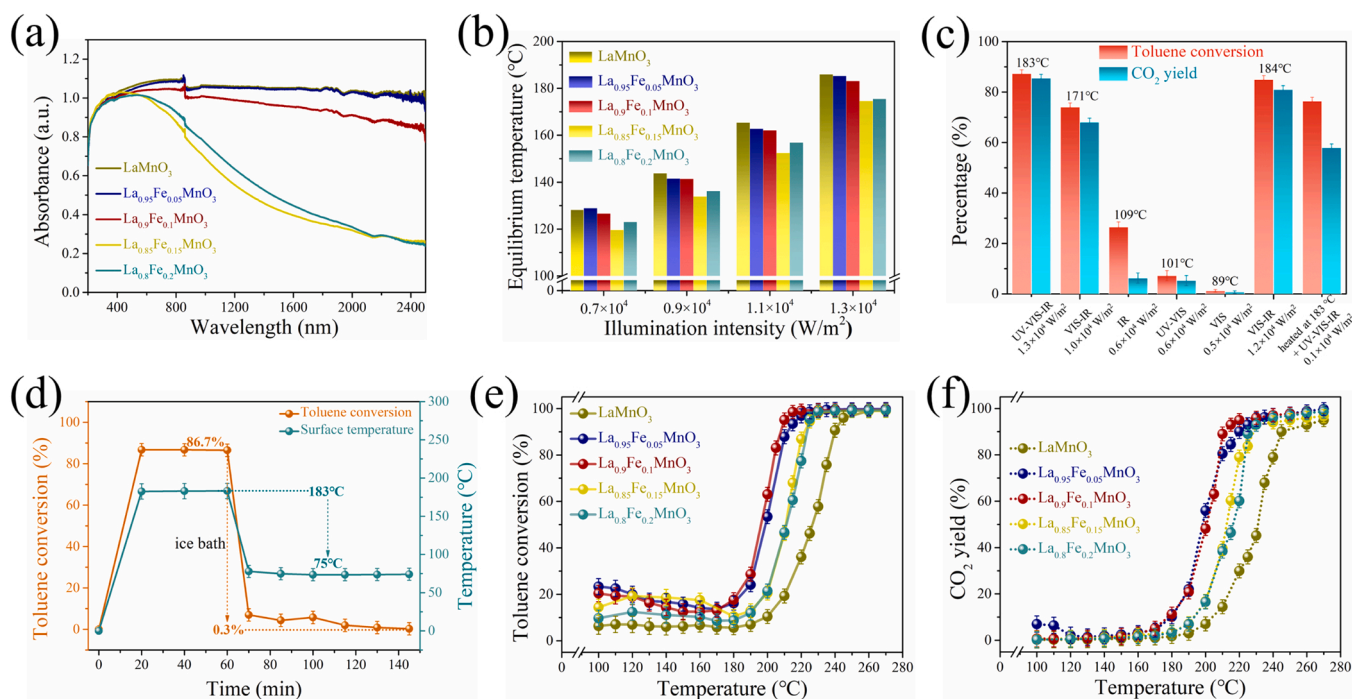


Fig. 2. (a) UV-VIS-IR DRS and (b) equilibrium temperature under light illumination of $\text{La}_{1-x}\text{Fe}_x\text{MnO}_3$ ($0 \leq x \leq 0.2$) samples. (c) The toluene conversion and CO_2 yield over $\text{La}_{0.9}\text{Fe}_{0.1}\text{MnO}_3$ under different wavelengths of light illumination (UV-VIS-IR, VIS-IR, IR, UV-VIS and VIS). (d) The variation of PTCO activity and surface temperature on $\text{La}_{0.9}\text{Fe}_{0.1}\text{MnO}_3$ under an ice water bath. (e) The toluene conversion and (f) CO_2 yield of $\text{La}_{1-x}\text{Fe}_x\text{MnO}_3$ ($0 \leq x \leq 0.2$) samples under traditional TCO reaction.

As we known, the short-wavelength UV light are the primary energy source for traditional PCO, while long-wavelength VIS and IR spectra can hardly excite the photogenerated carriers, their contribution to some redox reactions is mainly attributed to their thermal effects [16, 29]. To investigate whether the photothermal catalysis on $\text{La}_{0.9}\text{Fe}_{0.1}\text{MnO}_3$ has both PCO and TCO reactions going on simultaneously, we placed the cut-off filters (420 nm and/or 800 nm) between the Xe lamp and quartz window to subdivide the UV-VIS-IR light into VIS-IR, IR, UV-VIS and VIS regions, as shown in Fig. 2c. Obviously, the activity under VIS-IR light illumination was much higher than that of IR, UV-VIS and VIS light, but lower than UV-VIS-IR light. When enhancing the VIS-IR light intensity until the induced temperature was close to that of UV-VIS-IR light, the activity of the two differed little. It implied that the VIS-IR light played a more critical role, which provided the required heat energy to trigger the oxidation of toluene over $\text{La}_{0.9}\text{Fe}_{0.1}\text{MnO}_3$. When controlling the light intensity of VIS-IR, IR, UV-VIS and VIS consistent with the UV-VIS-IR light (Fig. S5), the activity showed a similar trend as that of Fig. 2c. Notably, under the relatively low UV-VIS-IR light illumination of $0.1 \times 10^4 \text{ W/m}^2$ and heated at 183 °C simultaneously, the activity showed a slight decrease, which suggested that light also had an activation effect and related with intensity. Interestingly, we placed it in an ice water bath, and further estimated the activity under light illumination of $1.3 \times 10^4 \text{ W/m}^2$ at low temperatures (Fig. 2d). It was found that the surface temperature was rapidly decreased from 183 °C to 77 °C due to the heat dissipation, which caused the toluene conversion plummeted and closed to 0%. Besides, there was feeble and no significant signal change of the photogenerated free radicals ($\cdot\text{OH}$, $\cdot\text{O}_2$) at dark and light illumination (Fig. S6). The results indicated that the contribution of traditional PCO was relatively insignificant or even negligible, and the activation of light acted on the basis of thermal effects.

In general, it can be argued that the excellent PTCO activity of $\text{La}_{0.9}\text{Fe}_{0.1}\text{MnO}_3$ originates from light-driven thermal catalysis with the activation of light. Owing to its excellent photothermal conversion ability, it can rapidly convert the absorbed light (mainly the VIS-IR

region) into heat, which increases the temperature of the local active sites, and suffices to induce the oxidation of toluene. Traditional TCO experiments also confirmed it. As presented in Fig. 2e and f, their sequence of TCO activity was consistent with that of PTCO, with the best performance of $\text{La}_{0.9}\text{Fe}_{0.1}\text{MnO}_3$ ($T_{90} = 208^\circ\text{C}$). And toluene began to be oxidized at around 180 °C, which meant that the equilibrium temperature (183 °C) of $\text{La}_{0.9}\text{Fe}_{0.1}\text{MnO}_3$ under UV-VIS-IR illumination could reach the light-off temperature for toluene oxidation. Thus, the light-driven thermal catalysis of toluene could occur. In addition, the equilibrium temperature of $\text{La}_{0.9}\text{Fe}_{0.1}\text{MnO}_3$ under IR illumination (109 °C) was much lower than the $T_{\text{light-off}}$ but still showed a certain activity, which further illustrated the existence of photoactivation. It was consistent with the report of Yu et al. [18]. In conclusion, the Fe doping and photoactivation effect both significantly impact the catalytic performance of LaMnO_3 . But how Fe doping and photoactivation affect the catalytic performance for toluene, as well as the specific reaction pathways and mechanisms, are subject to be illustrated by further detailed characterizations and DFT calculations.

3.3. The effect of Fe doping

3.3.1. Crystal phase structure

Fig. 3 shows the XRD patterns of $\text{La}_{1-x}\text{Fe}_x\text{MnO}_3$ ($0 \leq x \leq 0.2$) samples. The diffraction peaks located at about 22.9° , 32.6° , 40.2° , 46.8° , 52.7° , 58.2° , 68.3° , 73.2° , and 77.8° can be indexed to the (100), (110), (111), (200), (210), (211), (220), (300), and (310) crystal planes of LaMnO_3 (JCPDS PDF #75-440), which suggests the successful synthesis of a well single-phase LaMnO_3 perovskite. After Fe doping, there was no significant shift in the characteristic peaks, but became broader and weaker sequentially with increasing Fe content. It was indicated that Fe doping could suppress the crystallization of LaMnO_3 and lead to more non-crystalline phases [30], thus reducing the crystallite size (Table 1). Moreover, the cell volumes of $\text{La}_{1-x}\text{Fe}_x\text{MnO}_3$ ($347.61\text{--}348.57 \text{ \AA}^3$) were shown to be reduced than that of LaMnO_3 (349.26 \AA^3), which could be ascribed to the partial substitution of the smaller ionic radius of Fe^{3+}

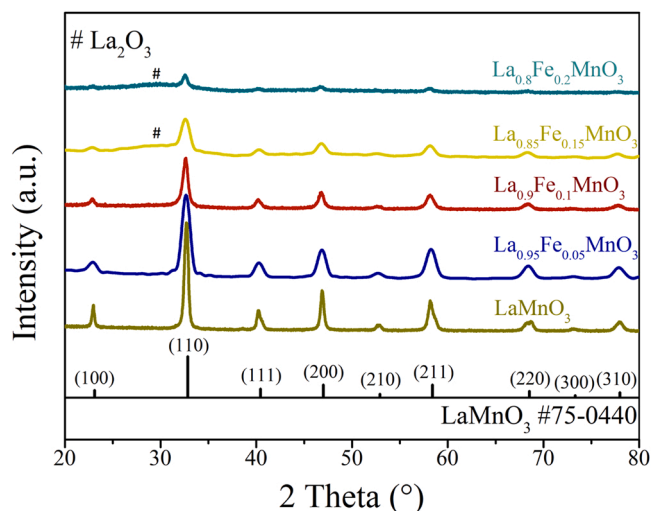


Fig. 3. XRD patterns of $\text{La}_{1-x}\text{Fe}_x\text{MnO}_3$ ($0 \leq x \leq 0.2$) samples.

(0.62 Å) for La^{3+} (1.17 Å), and lead to the cell lattice shrinkage and distortion [25,27]. It might further induce the generation of lattice defects [25]. Notably, no characteristic peaks of Fe species were observed, suggesting Fe cations might incorporate into the lattice of LaMnO_3 and were highly distributed [4]. And a newly weak diffraction peak located at 29.9° was detected on $\text{La}_{0.85}\text{Fe}_{0.15}\text{MnO}_3$ and $\text{La}_{0.8}\text{Fe}_{0.2}\text{MnO}_3$, which was assigned to the (101) lattice planes of hexagonal La_2O_3 (JCPDS PDF #74-2430). The presence of La_2O_3 impurity could attribute to the surface enrichment of La species during calcination, which discouraged the formation of the perovskite phase and led to the decrease in catalytic activity [31].

3.3.2. Morphological and textural properties

The morphologies of the samples were characterized by SEM, as depicted in Fig. S7. All samples have a bulk structure with spongy-like surface consisting of agglomerates and numerous pores, which favors the exposure of active sites. Such morphology is a consequence of the thermal decomposition of citric acid [32].

Fig. 4 presents the N_2 adsorption-desorption isotherms and pore size distribution curves. At the relative high-pressure ratio ($P/P_0 = 0.4\text{--}1.0$), all samples possess the typical IV isotherms with an H3 type hysteresis loop, which indicates the presence of mesoporous structures. And their particle sizes are basically clustered between 2 and 20 nm, which affirms this inference. Moreover, as shown in Table 1, with increased Fe content, the pore size of samples exhibited a decreasing trend (from 11.3 to 8.0 nm), suggesting the structure transformed from the stacked state to a loose state. While their specific surface area and pore volume were increased with Fe content, which was consistent with the XRD results and suggested the inhibition of crystallization [29]. Thereinto, $\text{La}_{0.8}\text{Fe}_{0.2}\text{MnO}_3$ showed the highest specific surface area ($43.5 \text{ m}^2/\text{g}$)

and pore volume ($0.106 \text{ cm}^3/\text{g}$), which was believed to benefit the adsorption/oxidation of toluene. However, the actual catalytic performance lacked a linear correlation with these textural properties, hence it might not be the dominant factor.

3.3.3. Surface chemical states

The XPS technique was utilized to evaluate the surface elementary composition and chemical states (La 3d, Mn 2p, and Fe 2p) of $\text{La}_{1-x}\text{Fe}_x\text{MnO}_3$ ($0 \leq x \leq 0.2$) samples (Fig. 5a), and the corresponding quantitative results were summarized in Table 2. It was worth mentioning that the (La+Fe)/Mn molar ratio of the $\text{La}_{1-x}\text{Fe}_x\text{MnO}_3$ ($0 \leq x \leq 0.2$) samples was approached 1.0, and the doping amount of Fe was also agreed well with the theoretical value (Table 1), which indicated that Fe successfully substituted La in the A-site instead of Mn in the B-site.

As shown in Fig. 5b, the spin-orbit splitting of La 3d is around 16.8 eV for all samples, suggesting the trivalent state of La [33]. Obviously, the peaks of La 3d_{5/2} and La 3d_{3/2} slightly shifted toward lower binding energy as the Fe content increased, which could be attributed to the elevated electron density around La cations [34]. And there was no significant change in the main peaks, implying La species possessed a relatively stable chemical environment. The Mn 2p spectra (Fig. 5c) is divided into two components, where the peaks at 641.8–641.9 eV correspond to Mn^{3+} species, and the peaks at 643.1–643.4 eV can be assigned to Mn^{4+} species [17]. As presented in Table 2, the $\text{Mn}^{4+}/\text{Mn}^{3+}$ molar ratio of $\text{La}_{1-x}\text{Fe}_x\text{MnO}_3$ ($0 \leq x \leq 0.2$) decreased to 0.65–0.69 by comparison with LaMnO_3 (1.17), implying that Fe doping had led to more low-valence Mn^{3+} . While the lower manganese state (Mn^{3+})

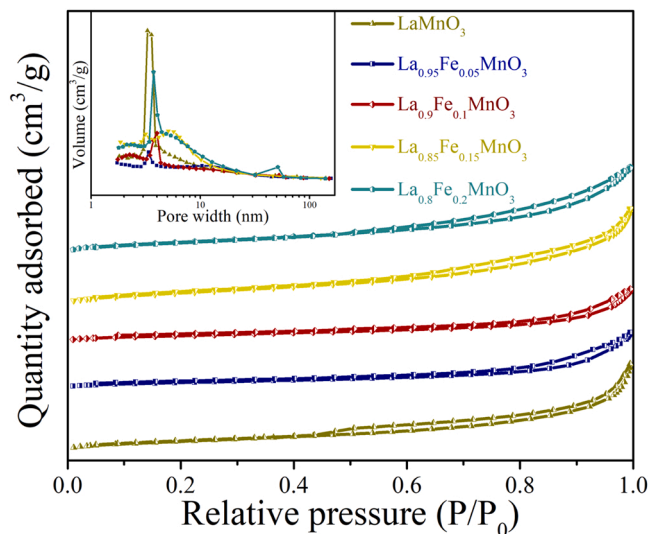


Fig. 4. N_2 adsorption-desorption isotherms and pore size distribution curves (inset) of $\text{La}_{1-x}\text{Fe}_x\text{MnO}_3$ ($0 \leq x \leq 0.2$) samples.

Table 1

The textural parameters of as-prepared samples (theoretical values in brackets).

Sample	Fe doping ^a (wt %)	Surface area ^b (m^2/g)	Pore volume ^c (cm^3/g)	Mean diameter ^c (nm)	Crystal size ^d (nm)	Lattice constant ^d (Å)			Cell volume ^d (\AA^3)
						a	b	c	
LaMnO_3	/	31.9	0.101	9.3	14.9	5.498	5.498	13.342	349.26
$\text{La}_{0.95}\text{Fe}_{0.05}\text{MnO}_3$	1.14 (1.18)	19.2	0.063	11.3	12.2	5.494	5.494	13.296	348.57
$\text{La}_{0.9}\text{Fe}_{0.1}\text{MnO}_3$	2.35(2.39)	28.6	0.064	9.7	11.6	5.489	5.489	13.291	348.38
$\text{La}_{0.85}\text{Fe}_{0.15}\text{MnO}_3$	3.41 (3.65)	36.1	0.104	9.0	11.6	5.485	5.485	13.306	347.96
$\text{La}_{0.8}\text{Fe}_{0.2}\text{MnO}_3$	4.81 (4.96)	43.5	0.106	8.0	10.5	5.482	5.482	13.307	347.61

^a The doping content of Fe was calculated by ICP-OES results.

^b The specific surface area was calculated based on N_2 adsorption-desorption by the BET method.

^c The pore volume and mean pore diameter was calculated by the BJH method.

^d The lattice parameter was obtained by XRD patterns.

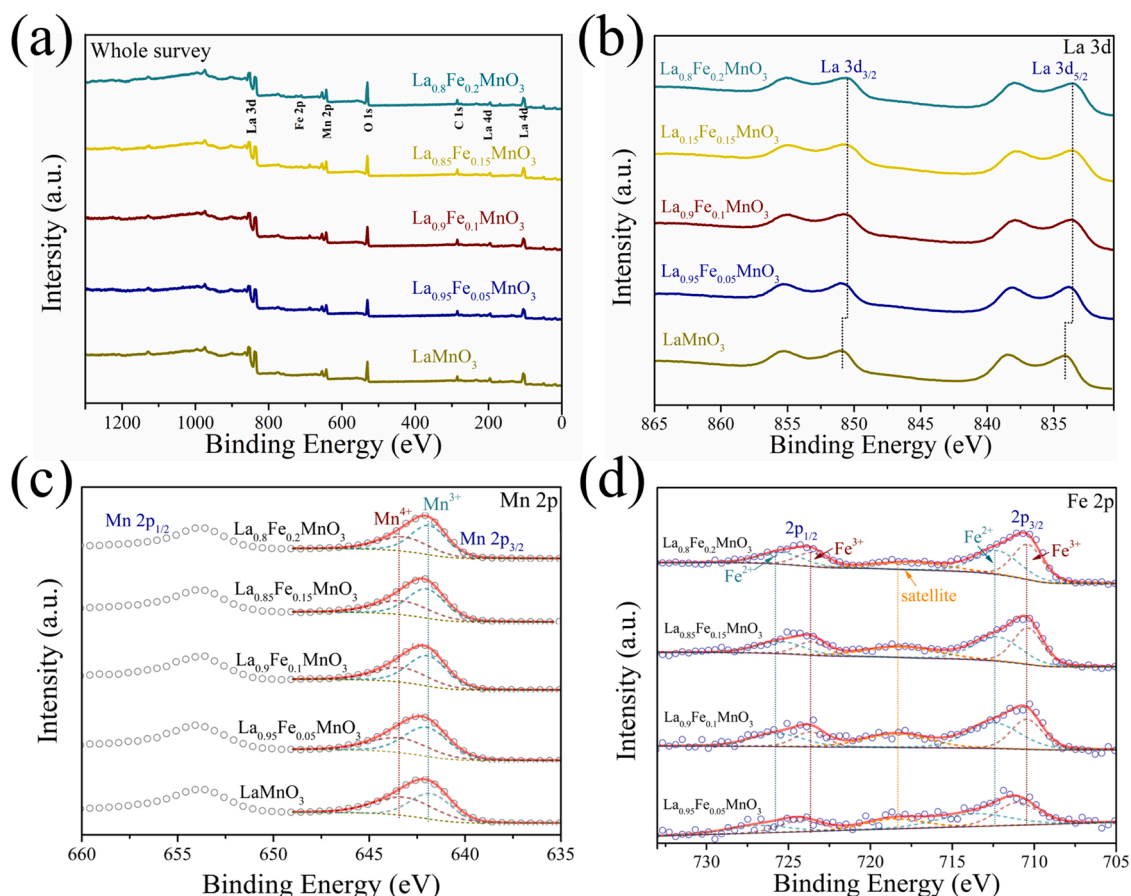


Fig. 5. (a) The full XPS spectra and high resolution XPS scans of (b) La 3d, (c) Mn 2p and (d) Fe 2p for $\text{La}_{1-x}\text{Fe}_x\text{MnO}_3$ ($0 \leq x \leq 0.2$) samples.

Table 2

The surface chemical states and quantitative results of as-prepared samples.

Sample	Molar ratio of (La+Fe)/Mn ^a	Mn 2p ^a	Fe 2p ^a	O 1 s ^a	O ₂ consumption (mmol/g) ^b				H ₂ consumption (mmol/g) ^c		
		Mn ⁴⁺ / Mn ³⁺	Fe ³⁺ / Fe ²⁺	O _{latt} / O _{ads}	100–300 °C	300–600 °C	600–900 °C	Total	100–500 °C	500–800 °C	Total
LaMnO ₃	1.03	1.17	/	1.13	0.056	0.342	0.551	0.949	1.822	1.670	3.492
La _{0.95} Fe _{0.05} MnO ₃	1.09	0.67	0.99	1.46	0.315	0.307	1.099	1.721	1.865	1.769	3.634
La _{0.9} Fe _{0.1} MnO ₃	0.97	0.65	1.45	1.48	0.073	0.657	1.418	2.148	3.760	0.796	4.756
La _{0.85} Fe _{0.15} MnO ₃	0.98	0.68	1.16	1.39	0.081	0.477	1.527	2.085	3.993	0.821	4.814
La _{0.8} Fe _{0.2} MnO ₃	0.93	0.69	1.08	0.98	0.076	0.504	1.510	2.09	4.077	0.808	4.885

^a Calculated by the XPS results.

^b O₂ consumption from O₂-TPD profiles.

^c H₂ consumption from H₂-TPR profiles.

present in the crystal can promote the mobility of lattice oxygen and affect the surface reactive oxygen species [35]. These properties were reported to facilitate the redox reaction of toluene [29].

For Fe species (Fig. 5d), two main asymmetric peaks are located at around 710.8 eV and 723.9 eV, which are assigned to the Fe 2p_{3/2} and Fe 2p_{1/2}, respectively (spin-orbital splitting of 13.2 eV) [25]. And the other peak at about 718.3 eV corresponds to the shake-up satellite, indicating the presence of surface Fe³⁺ [36]. The Fe 2p_{3/2} orbit can split into two peaks, which are attributed to Fe²⁺ (710.4–711.0 eV) and Fe³⁺ (712.2–713.7 eV), accordingly [37]. The valence state transformation of the Fe cations from +2 to +3 indicated a significant change in the electronic structure, which also verified the successful doping of Fe to the LaMnO₃ lattice [38]. Notably, the high-valence Fe³⁺ can act as the active site for toluene oxidation, and its concentration in La_{0.9}Fe_{0.1}MnO₃ is the highest of all samples (Fe³⁺/Fe²⁺=1.45). Combined with the decrease of Mn⁴⁺/Mn³⁺ after Fe doping, we speculated there was an

intense interaction between Fe and Mn species, which greatly accelerates electron transfer and meets the needs of multi-electron reaction (e.g., toluene oxidation). In addition, after PTCO or TCO reactions (Fig. S8), the peak position of surface Mn⁴⁺ and Fe³⁺ on La_{0.9}Fe_{0.1}MnO₃ moved to higher binding energy, and the ratio of Mn⁴⁺/Mn³⁺ and Fe³⁺/Fe²⁺ were differentially reduced (Table S3). The results suggest that the surface Mn⁴⁺ and Fe³⁺ as the active components are involved in the redox reaction of toluene.

3.3.4. Reactive oxygen species

Generally, reactive oxygen species are tightly involved in the adsorption/activation of VOCs molecules, especially lattice oxygen plays an essential role in the Mars-van-Krevelen mechanism for the oxidation of aromatic VOCs [17]. Accordingly, we applied the XPS, TPD, TPR techniques to reveal the types and properties of reactive oxygen species in the as-prepared samples. And DFT calculations were

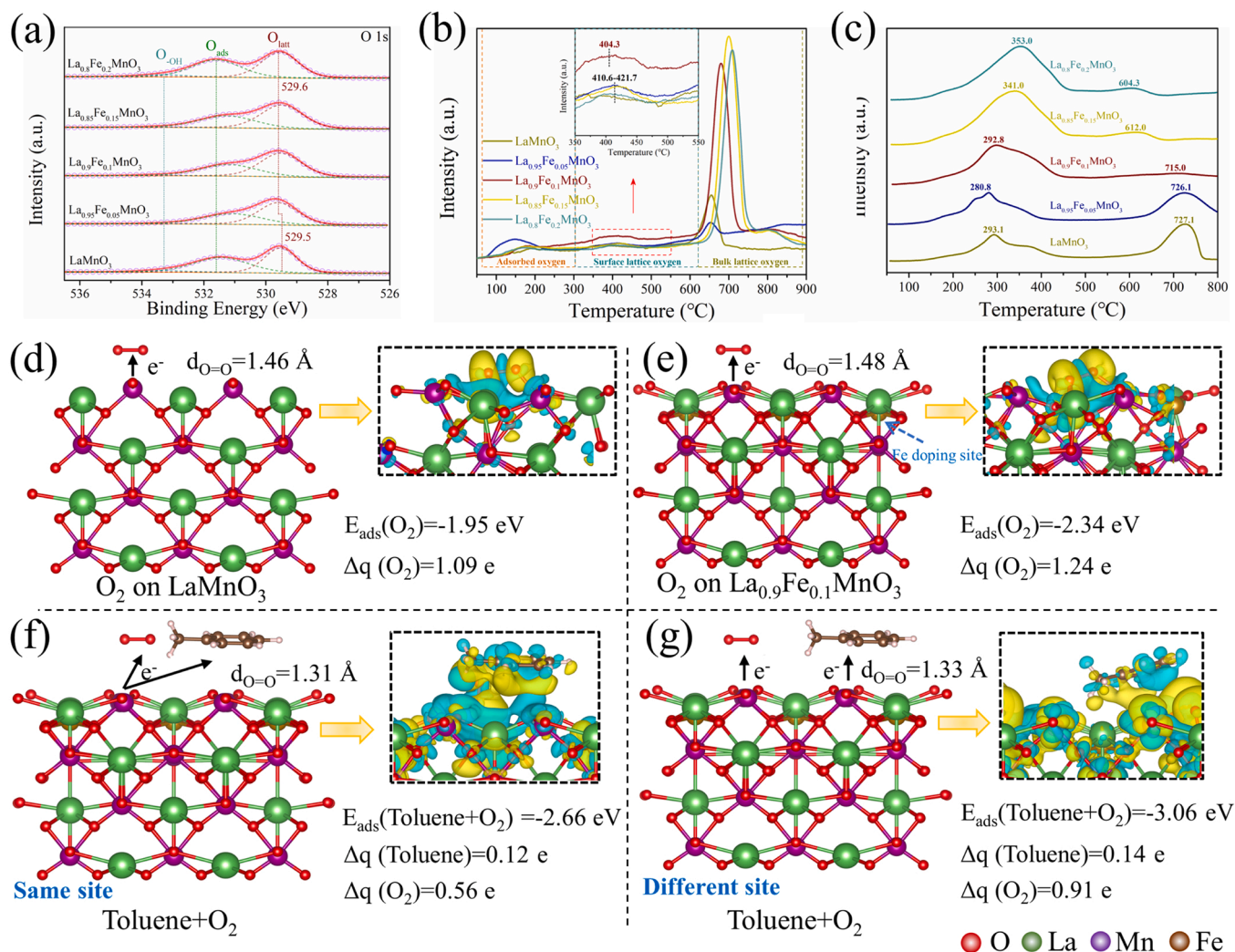


Fig. 6. (a) O 1s XPS spectra, (b) O₂-TPD profiles (the inset is an enlarged part from 350 °C to 550 °C), and (c) H₂-TPR profiles of $\text{La}_{1-x}\text{Fe}_x\text{MnO}_3$ ($0 \leq x \leq 0.2$) samples. The O₂ adsorption simulation of (d) LaMnO_3 and (e) $\text{La}_{0.9}\text{Fe}_{0.1}\text{MnO}_3$. The O₂ and toluene co-adsorption at same (f) and different sites (g) simulation of $\text{La}_{0.9}\text{Fe}_{0.1}\text{MnO}_3$. The isosurfaces are set to $0.002 \text{ eV} \cdot \text{\AA}^{-3}$.

conducted to investigate the effect of O₂ for adsorption/activation of toluene.

As shown in Fig. 6a, the O 1s spectra are used to identify the surface oxygen species. The peaks at around 529.5–529.6 eV, 531.1–531.6 eV, and 533.4 eV can be assigned to surface lattice oxygen (O_{latt}), surface adsorbed oxygen (O_{ads}), and hydroxyl/adsorbed molecular water (O_{OH}), respectively [29]. The associated quantitative results are summarized in Table 2. As a symbol of the intrinsic relationship between reducibility and oxygen species, the atomic ratio of $\text{O}_{\text{latt}}/\text{O}_{\text{ads}}$ was increased substantially after Fe doping, which might be related to the valence variation of the metal species [30]. Thereinto, the $\text{La}_{0.9}\text{Fe}_{0.1}\text{MnO}_3$ showed the highest value of 1.48 compared to LaMnO_3 (1.13), demonstrating that the Fe had a significant impact on the reactive oxygen species. Moreover, the peaks of O_{latt} inclined to slightly shift toward higher binding energy, which could ascribe to the decrease in electron density around O_{latt} [39]. The O_{latt} atoms may bond less tightly in the structure, and lead to higher mobility [40].

O₂-TPD was applied to further investigate the mobility of oxygen species. As presented in Fig. 6b, which are divided into three regions. In the low-temperature region of 50–300 °C, the oxygen desorption peaks belong to the chemisorbed oxygen species (O_2^- or O_2^{2-}) and physisorbed molecular oxygen [41]. For 300–600 °C, the peaks can be assigned to

the desorption of surface O_{latt} species (O^{2-}) generated by lattice defects [31]. At the high-temperature region (600–900 °C), the peaks are associated with the bulk O_{latt} species, which are usually accompanied by a decreased valence of the B-site metal cations in perovskite oxides [42]. Since the reaction usually proceeds at a relatively low temperature, the oxygen desorption behavior at low/middle temperatures deserves more attention. For $\text{La}_{0.95}\text{Fe}_{0.05}\text{MnO}_3$, the desorption area at the low temperature of 100–300 °C was enlarged significantly, implying a higher O_{ads} content. It is believed that the O_{ads} with strongly electrophilic can attack organic molecules readily [43]. Thereby, the $\text{La}_{0.95}\text{Fe}_{0.05}\text{MnO}_3$ could perform better at low light intensity (low temperatures). As for surface O_{latt} species, their desorption temperature is well correlated with mobility [17]. At the middle-temperature region (300–600 °C), $\text{La}_{0.9}\text{Fe}_{0.1}\text{MnO}_3$ exhibited a larger amount and lower desorption temperature than other samples, which indicated that the moderate doping of Fe could enhance the mobility of surface O_{latt} and accelerate oxygen species migration from subsurface to surface [17,29]. It was in agreement with the results of XPS. The enhanced mobility and amount of surface O_{latt} may be a major factor contributing to the promising PTCO performance on $\text{La}_{0.9}\text{Fe}_{0.1}\text{MnO}_3$. Moreover, as listed in Table 2, the total O₂ desorption of LaMnO_3 (0.949 mmol/g) was much less than that of Fe doped samples. The $\text{La}_{0.9}\text{Fe}_{0.1}\text{MnO}_3$ had the most O₂ consumption of

2.148 mmol/g, suggesting a larger amount of reactive oxygen species. It is probably explained by the fact that the doping of Fe can induce lattice defects that promote the mobility and/or activation of oxygen species [25].

TPR experiment is performed to study the reactivity of oxygen species. The H₂-TPR profiles are given in Fig. 6c. It is worth mentioning that La³⁺ is hardly reduced below 1000 °C, thus the discussion is based on the reduction of Mn and Fe cations. There are two clear H₂ consumption peaks in LaMnO₃, where the peak at low temperatures (100–500 °C) corresponds to the consumption of a small amount surface adsorbed oxygen, accompanied by the reduction of Mn⁴⁺ to Mn³⁺ and a single electron reduction of Mn³⁺ (located in a highly coordination-unsaturated microenvironment) to Mn²⁺, while the second reduction peak (500–800 °C) is attributed to the reduction of the Mn³⁺ left in the LaMnO₃ lattice to Mn²⁺ [44]. After Fe doping, new reduction processes were occurring, which could be correlated with the surface Fe³⁺ to Fe²⁺ between 100 and 500 °C, and bulk Fe³⁺ to Fe²⁺, Fe²⁺ to Fe⁰ at temperatures exceeding 500 °C [4]. Obviously, the first reduction peak tended to shift toward higher temperatures with increased Fe content. Compared with LaMnO₃, La_{0.95}Fe_{0.05}MnO₃ and La_{0.9}Fe_{0.1}MnO₃ both exhibited a lower reduction temperature. It could be considered that the moderate doping of Fe improved the mobility of O_{latt} species [45], consistent with the results of XPS and O₂-TPD. Moreover, the H₂ consumption at low temperatures is informative for exploring the reducibility. As given in Table 2, the H₂ consumption of La_{0.9}Fe_{0.1}MnO₃ was significantly increased to 3.760 mmol/g between 100 and 500 °C, compared to that of La_{0.95}Fe_{0.05}MnO₃ with 1.865 mmol/g. It is commonly believed to be related to highly mobilized oxygen species, which explained the rapid generation of surface sites for H₂ adsorption [46]. And some reactive oxygen species (e.g., surface O_{latt}) are closely related to catalytic activity, which is mainly reflected by low-temperature reducibility. Therefore, La_{0.9}Fe_{0.1}MnO₃ with better mobility and quantity of surface O_{latt} may have stronger low-temperature reducibility despite its slightly higher reduction temperature than La_{0.95}Fe_{0.05}MnO₃.

In a typical VOCs oxidation process, the reoxidation of reduced metal species is well associated with the replenishment of surface O_{latt} from free O₂ [47]. To pursue long-term reaction durability, the availability of timely replenishment of consumed reactive oxygen species also needs to be evaluated. While O₂ molecules as the main source of oxygen species, are essential for VOCs oxidation. Thus, a comparison of O₂ simulated adsorption processes of LaMnO₃ and La_{0.9}Fe_{0.1}MnO₃ was performed by DFT calculations. As displayed in Fig. 6d and e, the absolute value of adsorption energy (*E*_{ads}) on La_{0.9}Fe_{0.1}MnO₃ (−2.34 eV) was much higher than LaMnO₃ (−1.95 eV), and the O–O bond length of O₂ on La_{0.9}Fe_{0.1}MnO₃ was extended to 1.48 Å, slightly longer than that on LaMnO₃ (1.46 Å). The results illustrate that O₂ molecules are more likely activated on La_{0.9}Fe_{0.1}MnO₃. Moreover, the electronic interaction between the O₂ and La_{0.9}Fe_{0.1}MnO₃ was stronger than LaMnO₃ from the differential charge density. And Bader charge calculation also confirmed this, the transferred charge (Δq) of O₂ on La_{0.9}Fe_{0.1}MnO₃ was 1.24 e, whereas that of LaMnO₃ was 1.09 e, implying that the O₂ obtained more electrons from La_{0.9}Fe_{0.1}MnO₃. Therefore, the charge transfer is easier between the O₂ and La_{0.9}Fe_{0.1}MnO₃. Combined with the stronger O₂ adsorption and activation, it is reasonable to speculate that the moderate doping of Fe will facilitate the formation and regeneration of reactive oxygen species, thus replenishing the consumed O_{latt} species and perpetuating reactions [47]. Furthermore, we investigated the co-absorption of O₂ and toluene on La_{0.9}Fe_{0.1}MnO₃ (Fig. 6f and g). As compared to separate absorption of O₂ (Fig. 6e) and toluene (Fig. S9), whether co-adsorbed of O₂ with toluene at the same sites or different sites, it was obvious that the presence of O₂ promoted the adsorption/activation of toluene. Notably, when co-adsorbed at different sites, the *E*_{ads} was much higher and electronic interaction (Δq , differential charge density) was more intense than that of at same sites, which might attribute to the competition absorption between O₂ and toluene. In fact,

when O₂ and toluene were adsorbed simultaneously, the electron transfer between O₂ and sample was reduced (especially co-adsorbed at same sites, the Δq decreased significantly from 1.24 e to 0.56 e), and this portion might contribute to the electronic interaction between toluene and sample (Δq (Toluene) was increased from 0.09 e to 0.12 e and 0.14 e), which could further promote the adsorption/activation of toluene.

3.4. The effect of photoactivation

In fact, in addition to the Fe doping, the photoactivation effect induced by light was also reported to affect the reactive oxygen species [18,29]. To further investigate the photoactivation effect, some characterizations and DFT calculations were performed.

As shown in Fig. 7a, the O peaks shifted toward higher binding energy after PTCO reaction, suggesting the O_{latt} was effectively activated [39]. Moreover, the O_{latt} was more significantly consumed after PTCO reaction, and the relative amount of O_{ads} was also found more than that of TCO (Table S3). In general, the generation of surface O_{ads} is usually associated with the adsorption of gaseous O₂, and it contributed to the replenishment of consumed O_{latt} species [47]. Yu et al. [29] reported that the photoactivation effect could activate more gaseous O₂ molecules, thus replenishing the surface O_{latt}. Therefore, it is reasonable to assume that light has a positive impact on activating oxygen species.

CO-TPR under illumination or at dark was also used to study the photoactivation effect. As displayed in Fig. 7b, a broad TPR peak appeared around 250 °C, which could be ascribed to the oxidation of CO by surface O_{latt} [48]. Obviously, the peak shifted to lower temperature under illumination, suggesting that the activity of O_{latt} was enhanced due to photoactivation. In addition, the CO consumption of La_{0.9}Fe_{0.1}MnO₃ was significantly increased from 247.0 μmol/g at dark to 311.7 μmol/g under illumination, which indicated that the light could activate more O_{latt} species to be involved in oxidation reactions.

DFT calculations were also performed to study the effect of light illumination on the O_{latt} activity over La_{0.9}Fe_{0.1}MnO₃ (Fig. 7c). Generally, the visible light absorption of metal oxides derived from the *d*-*d* transition, which induces the materials in the ground state to the excited state [49]. Accordingly, we applied the constrained occupancy DFT approach, and changed the *d* electron number in down and up spin components to calculate the energy of removing one O atom from materials in the excited state [50]. It could be observed that the ΔE of removing one O atom from La_{0.9}Fe_{0.1}MnO₃ was 0.665 eV, respectively, which was much lower than that of the ground state (2.092 eV). And that LaMnO₃ showed the same phenomenon (Fig. S10). It suggests that the activity of O_{latt} is enhanced by visible light, in agreement with the result of CO-TPR.

Furthermore, to investigate the catalytic behavior of the O_{latt} activated by light, in situ DRIFT was firstly carried out in Toluene/N₂ atmosphere. As observed from Fig. 8a, some typical characteristic absorbance bands of toluene appeared, and their intensity slightly increased with time. The peaks at around 1619, 1551, and 1464 cm^{−1} are ascribed to the C=C stretching vibration of the aromatic ring [51]. The bands at 2938 and 2874 cm^{−1} are from the C–H symmetric and asymmetric vibration of methylene (–CH₂) [52]. While under light illumination, these typical peaks were weakened or disappeared immediately. And some new peaks appear at 1594 and 1416 cm^{−1} are ascribed to the C=O stretching vibration of aldehydic species and –COO– stretch modes of benzoate species, respectively [29], demonstrating the formation of typical intermediates in toluene oxidation. In addition, the new peak at 1315 cm^{−1} is regarded as the maleic acid and maleic anhydride, and the band located at 1735 cm^{−1} belonging to chain fatty acid is also detected, which are important intermediates in the ring-opening process of toluene [11]. The results suggest that the oxidation of toluene can be conducted by using surface O_{latt} species activated by light in absence of O₂. However, since the O_{latt} is not available for timely replenishment, it is difficult to achieve the deep oxidation of toluene. To further discuss the pathway of toluene

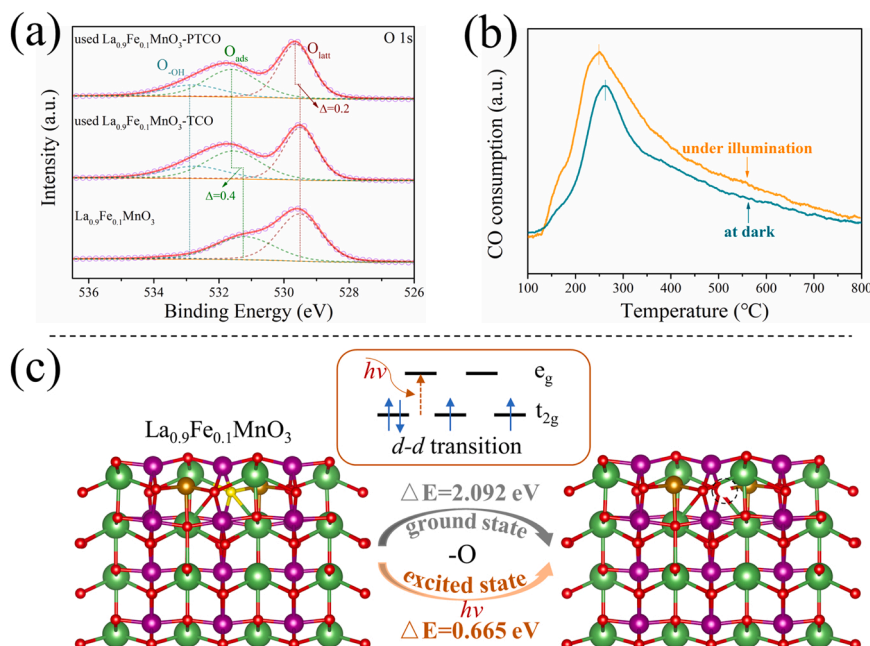


Fig. 7. (a) O 1s XPS spectra of fresh and used $\text{La}_{0.9}\text{Fe}_{0.1}\text{MnO}_3$ after PTCO or TCO reactions. (b) CO-TPR profile of $\text{La}_{0.9}\text{Fe}_{0.1}\text{MnO}_3$ under Xe lamp illumination and at dark. (c) Calculated energy of removing one O atom (yellow sphere) from the $\text{La}_{0.9}\text{Fe}_{0.1}\text{MnO}_3$ in the ground or excited states. (PTCO reaction condition: 500 ppm toluene, 20 vol% O_2/N_2 , light intensity = $1.3 \times 10^4 \text{ W/m}^2$; TCO reaction condition: 500 ppm toluene, 20 vol% O_2/N_2 , 183 °C).

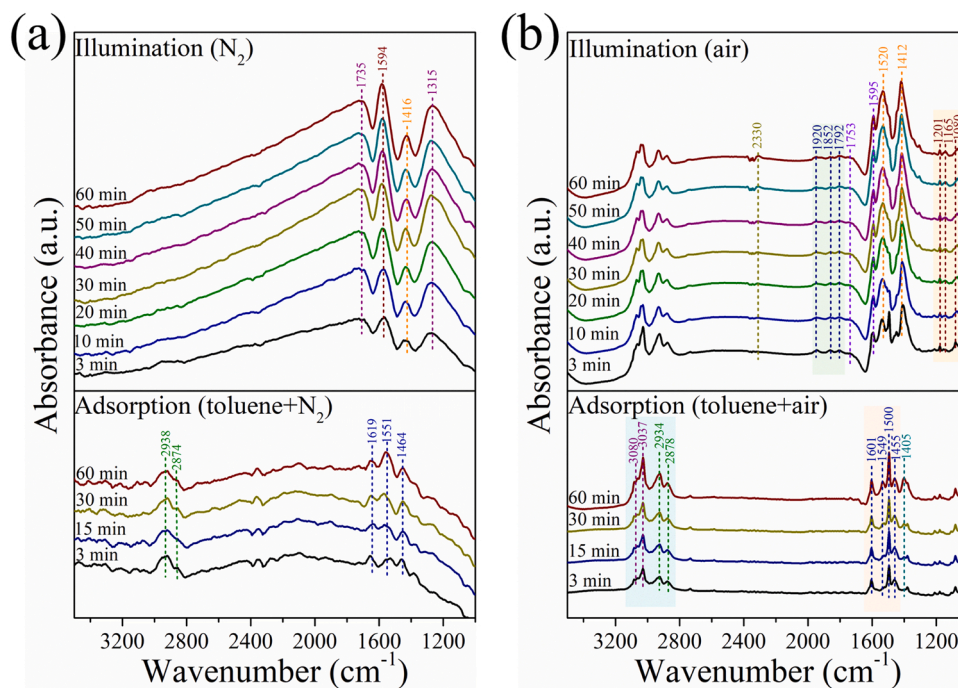


Fig. 8. In situ DRIFT spectra of toluene adsorption and oxidation on $\text{La}_{0.9}\text{Fe}_{0.1}\text{MnO}_3$ in (a) N_2 and (b) air.

degradation, it is essential to investigate the adsorption and oxidation behavior in the air atmosphere. As shown in Fig. 8b, after introducing toluene, the typical aromatic ring vibrations at 1601, 1549, 1500 and 1455 cm^{-1} were observed immediately, and their intensity increased with time [43,51]. In the C–H stretching region ($3100\text{--}2850 \text{ cm}^{-1}$), the bands at 3080 and 3037 cm^{-1} belong to the aromatic ring, and the bands at 2934 and 2878 cm^{-1} are attributed to methylene ($-\text{CH}_2$). Moreover, the peak corresponding to the bending vibration of CH_2 is detected at 1405 cm^{-1} [53]. These results suggest that the toluene can be more strongly adsorbed on the catalyst through its methyl group in air. While

under light illumination, the weak bands at 1920, 1852, and 1792 cm^{-1} associated with the maleic anhydride are observed, and also detect the characteristic band of final product CO_2 at 2330 cm^{-1} , which illustrates the occurrence of oxidation reactions [54]. In contrast, the spectra remain almost unchanged after heating to 183 °C (agreeing with the light-induced equilibrium temperature) in the dark (Fig. S11). The results revealed that light could effectively activate O_{latt} species to be involved in the oxidation of toluene.

Moreover, similar to the experiments in the N_2 atmosphere, new characteristic bands of some important intermediates appeared. The

weak bands at 1201, 1165, and 1080 cm^{-1} are regarded as the C–O stretching vibration of benzyl alcohol [11,51]. The strong bands at 1520 and 1412 cm^{-1} can be assigned to the –COO– stretching vibrations of benzoate species, demonstrating the formation of benzoic acid directly [55]. The bands at 1753 and 1595 cm^{-1} assigned to aldehydic species indicate the formation of benzaldehyde [56]. Notably, these bands (especially the bands belonging to the benzoate species) continued to increase and became the prominent peaks, which suggested that benzyl alcohol, benzoic acid, and benzaldehyde are the key intermediates in the deep oxidation of toluene to CO_2 and H_2O , and toluene oxidation follows the benzoate reaction route [57]. In the presence of O_2 , consumed O_{latt} gets timely replenishment, thus the oxidation pathway of toluene is slightly changed, allowing toluene to be degraded more deeply.

Moreover, to better understand the role of O_{latt} on toluene oxidation, the $^{18}\text{O}_2$ isotope experiment was further carried out under light illumination, and the reaction products (C^{16}O_2 , $\text{C}^{16}\text{O}^{18}\text{O}$, C^{18}O_2) were detected (Fig. 9a). Obviously, the C^{18}O_2 was generated abundantly, meanwhile the C^{16}O_2 was also produced due to the involvement of O_{latt} . However, as the reaction proceeded, the O_{ads} was consumed and the peak of C^{18}O_2 almost disappeared, while C^{16}O_2 was still detected, which confirmed that O_{latt} was activated and continuously involved in toluene oxidation under illumination. Notably, there was no detectable peak of $\text{C}^{16}\text{O}^{18}\text{O}$, suggesting that the O_{ads} might preferentially oxidize toluene over the replenishment of O_{latt} in absence of O_2 .

3.5. Reaction mechanism

It is well known that the ring-opening process is the rate-determining step of toluene oxidation. Thus, clarifying the ring-opening step of toluene is the highlight of exploring the plausible mechanism. Many studies have proposed that the reaction begins from the oxidation of methyl groups and follow the path of toluene \rightarrow benzyl alcohol \rightarrow benzaldehyde \rightarrow benzoic acid [58]. To confirm this inference, the stepwise energy barriers of these intermediates on LaMnO_3 and $\text{La}_{0.9}\text{Fe}_{0.1}\text{MnO}_3$ were calculated (Fig. S12). Obviously, the conversion of toluene to benzoic acid exhibited a significant heat release trend on samples, suggesting that toluene was more preferentially converted to benzoic acid. In addition, the toluene conversion over $\text{La}_{0.9}\text{Fe}_{0.1}\text{MnO}_3$ was much more thermodynamically favorable than LaMnO_3 , which accounted for the higher activity of $\text{La}_{0.9}\text{Fe}_{0.1}\text{MnO}_3$.

Based on the results of in situ DRIFT, $^{18}\text{O}_2$ isotope tracing experiment, and DFT calculations, the reaction mechanism in absence of O_2 and in presence of O_2 is presumed and presented in Fig. 9b. Toluene is first adsorbed onto the catalyst by reacting with the reactive oxygen species via the C–H bond of the methyl group to form an intermediate ($\text{C}_6\text{H}_5-\text{CH}_2-\text{O}$). In absence of O_2 , the catalyst gives up its O_{latt} to oxidize toluene to benzaldehyde directly, and further transform to

benzoic acid and maleic anhydride. Meanwhile, the active components (Mn^{4+} and Fe^{3+}) are reduced, and new surface oxygen vacancies are produced. Since the lack of O_2 , the produced oxygen vacancies can be replenished by the movement of O_{latt} from the catalyst bulk, thus enabling the whole reaction cycle to proceed. The enhanced reducibility by Fe doping and the activated O_{latt} by photoactivation significantly promote this process. It showed a typical MvK mechanism. In presence of O_2 , the adsorbed toluene follows the rapid dehydrogenation step as benzyl alcohol, benzaldehyde, and benzoic acid. The initiated benzoate then proceeds through a ring-opening step to form maleic anhydride, which is further oxidized and finally CO_2 and H_2O [51]. Notably, the oxygen vacancies formed during the oxidation under oxygen-rich conditions can be more readily replenished by gaseous O_2 rather than bulk O_{latt} due to the easier activation of gaseous O_2 on the catalyst surface [43]. And there are other active electrophilic oxygen species (e.g., O_2^- , O^-) formed in presence of O_2 [59]. Since the nature of reactive oxygen species strongly influences product selectivity [60], it differs from that of absence of O_2 , the adsorbed toluene is firstly oxidized to benzyl alcohol.

3.6. The co-effect of Fe doping and photoactivation for reactions

In this work, Fe doping is demonstrated to improve the mobility and amount of surface O_{latt} species, as well as low-temperature reducibility by XPS, O_2 -TPD and H_2 -TPR characterizations, while the photoactivation effect has also been shown to be effective in activating surface O_{latt} species by CO-TPR, in situ DRIFT, $^{18}\text{O}_2$ isotope tracing experiment and DFT calculations. The two have synergistically promoted the oxidation of toluene. From the perspective of practical applications, in addition to activity, we also investigated the co-effect of Fe doping and photoactivation on other aspects, such as resistance and durability.

3.6.1. The resistance to complex gas components

O_2 is indispensable in catalytic reactions. However, O_2 concentration may vary from field to field in the actual exhaust gas, it is meaningful to examine the effect of varying O_2 concentrations on the catalytic activity. To explore the impact of photoactivation more scientifically, we set the temperature of TCO to 208 $^\circ\text{C}$, in which the activity is close to that of PTCO. As displayed in Fig. 10a, with the O_2 concentration dropped to 6%, the samples under PTCO reaction showed only a slight decrease, whereas the performance of $\text{La}_{0.9}\text{Fe}_{0.1}\text{MnO}_3$ -TCO was inhibited (from 87.7% to 74.9%). Interestingly, we found there were more intermediates deposited on used- $\text{La}_{0.9}\text{Fe}_{0.1}\text{MnO}_3$ -TCO via FTIR analysis, which could mask active sites thus resulting in the decrease of activity (Fig. S13 and Text S5). While the light activated more O_{latt} species to participate in the deep oxidation of toluene, which reduced the accumulation of intermediates and exposed more active sites, enabling the activity to be

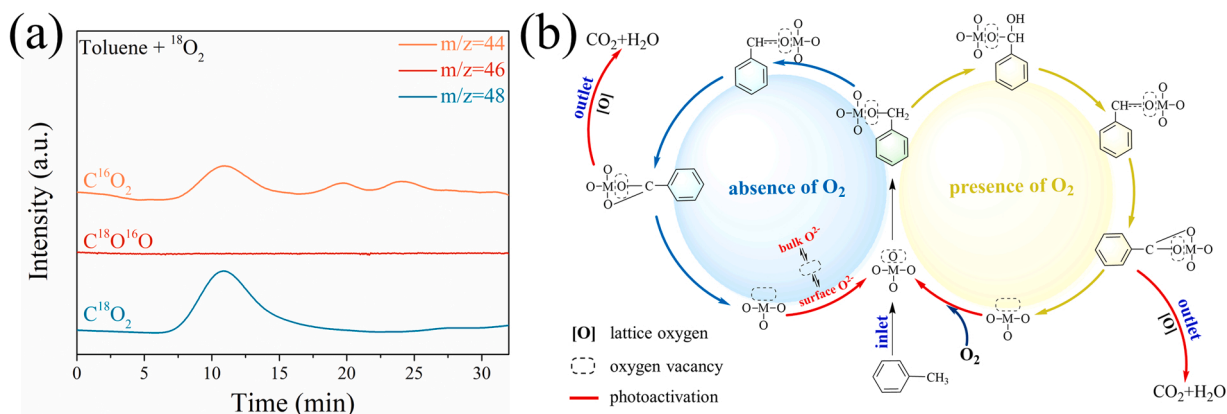


Fig. 9. (a) MS results of evolution of CO_2 in $^{18}\text{O}_2$ isotope tracing experiment over $\text{La}_{0.9}\text{Fe}_{0.1}\text{MnO}_3$ under illumination. (b) The plausible pathways and mechanisms of toluene oxidation in absence of O_2 and in presence of O_2 .

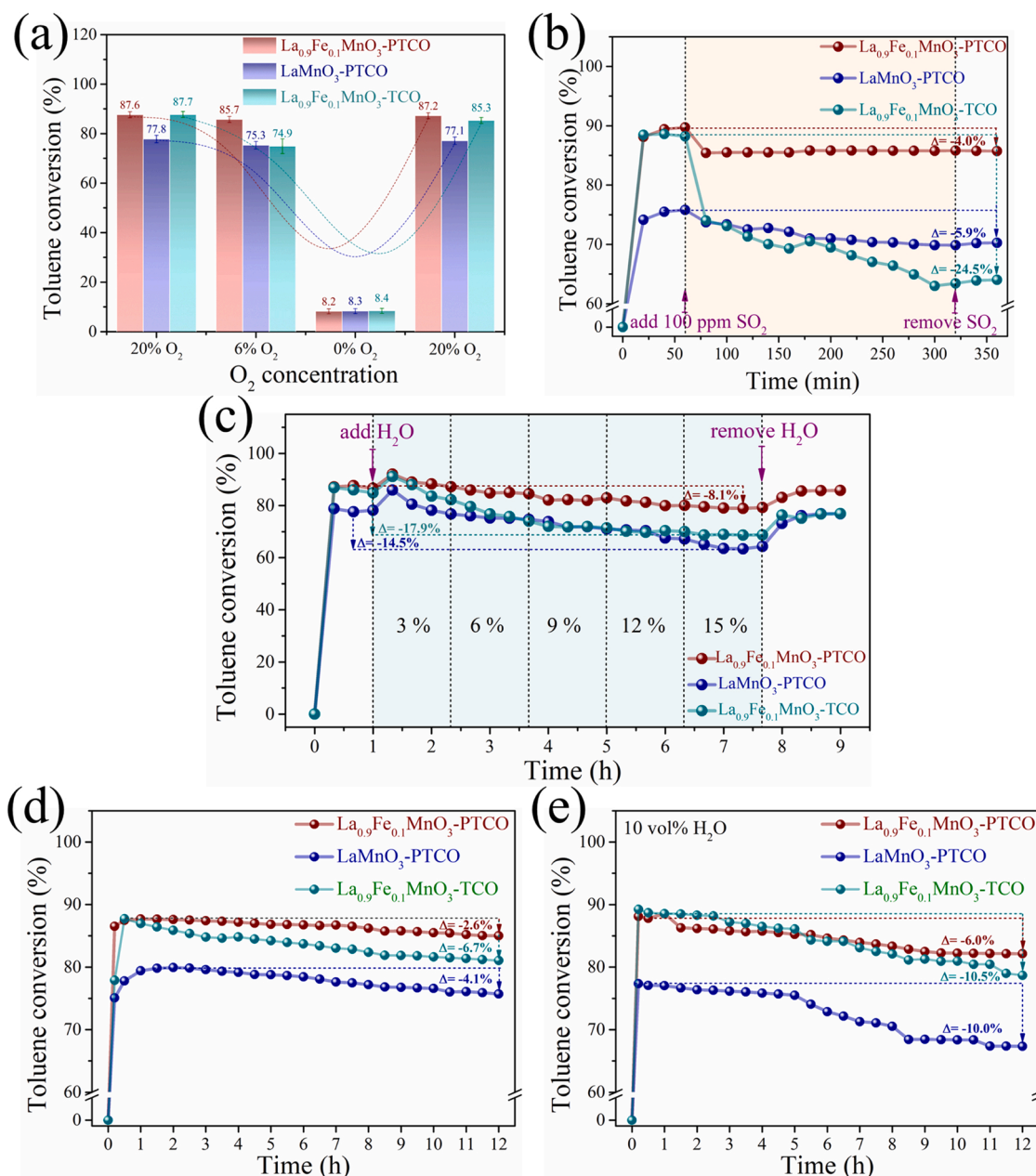


Fig. 10. Effect of (a) O_2 concentration, (b) SO_2 and (c) water vapor on toluene conversion. of $\text{La}_{0.9}\text{Fe}_{0.1}\text{MnO}_3\text{-PTCO}$, $\text{LaMnO}_3\text{-PTCO}$, and $\text{La}_{0.9}\text{Fe}_{0.1}\text{MnO}_3\text{-TCO}$. The comparative durability experiments (d) in absence and (e) in presence of water vapor. (PTCO reaction condition: 500 ppm toluene, 20 vol% O_2/N_2 , light intensity = $1.3 \times 10^4 \text{ W/m}^2$; TCO reaction condition: 500 ppm toluene, 20 vol% O_2/N_2 , 208 °C).

maintained. Additionally, in the absence of O_2 , all samples exhibited relatively low activity, while they were recovered as the O_2 concentration increased again to 20%. Notably, the $\text{La}_{0.9}\text{Fe}_{0.1}\text{MnO}_3$ still achieved 87.2% toluene conversion at 6 vol% O_2 under illumination, illustrating its practical applicability in low O_2 conditions, such as coal flue gas.

In general, industrial exhaust contains various components, such as SO_2 and H_2O . Thereby, we investigated the resistance of the samples to SO_2 and H_2O . After introducing 100 ppm SO_2 into the reaction system, the toluene conversion of all samples showed a significant and irreversible decrease (Fig. 10b). Such a negative effect may be attributed to the cumulative adsorption of SO_2 and the formation of sulfur/sulfate deposition at active sites [61]. Thereinto, the $\text{La}_{0.9}\text{Fe}_{0.1}\text{MnO}_3\text{-TCO}$ activity ($\Delta = -24.5\%$) dropped more dramatically than that of $\text{La}_{0.9}\text{Fe}_{0.1}\text{MnO}_3\text{-PTCO}$ ($\Delta = -4.0\%$) and $\text{LaMnO}_3\text{-PTCO}$ ($\Delta = -5.9\%$). It implies that Fe doping and photoactivation can improve the resistance of the catalyst to SO_2 to some extent, where photoactivation contributes

more. Instead of SO_2 , the deactivation induced by H_2O is reversible. As displayed in Fig. 10c, with continuously increasing the H_2O concentrations, the toluene conversion exhibited a transient increase and then a slow decrease in all samples. After cutting off H_2O , the activity of all samples was reversible. The transient increase of activity is probably due to the activation effect of H_2O on surface adsorbed oxygen species (O_2 , O_2^- etc.), which reacted according to the equation: O_2 , $\text{O}_2^- + \text{H}_2\text{O} \rightarrow 2 \text{O}^* + 2 \text{OH}$ [62]. This may favor the adsorption and activation of toluene, however, as the H_2O concentration increases from 3 to 15 vol%, the excess H_2O molecules will competitively occupy the active sites and continue to accumulate, which results in a continuous decrease in activity. In contrast, the $\text{La}_{0.9}\text{Fe}_{0.1}\text{MnO}_3\text{-PTCO}$ exhibited more superior H_2O resistance with only a slight decrease of 8.1%, whereas that of $\text{LaMnO}_3\text{-PTCO}$ and $\text{La}_{0.9}\text{Fe}_{0.1}\text{MnO}_3\text{-TCO}$ decreased 14.5% and 17.9%, respectively. In other words, Fe doping and photoactivation effect

synergistically improve the resistance to H₂O.

3.6.2. The durability

As mentioned in Section 3.1, the La_{0.9}Fe_{0.1}MnO₃ exhibited outstanding durability in a 34 h toluene stream. To clarify the effect of Fe doping and photoactivation on durability, a comparative experiment with 12 h toluene flow was conducted in presence or in absence of water vapor. As shown in Fig. 10d and e, in absence of water vapor, the activity of all samples had varying decreases as the sequence of La_{0.9}Fe_{0.1}MnO₃-PTCO ($\Delta = -2.6\%$) < LaMnO₃-PTCO ($\Delta = -4.1\%$) < La_{0.9}Fe_{0.1}MnO₃-TCO ($\Delta = -6.7\%$). And the crystal phase structure of La_{0.9}Fe_{0.1}MnO₃ could be well maintained after reactions (Fig. S14). Likewise, the activity of samples followed the same order in presence of water vapor (10 vol% H₂O): La_{0.9}Fe_{0.1}MnO₃-PTCO ($\Delta = -6.0\%$) < LaMnO₃-PTCO ($\Delta = -10.0\%$) < La_{0.9}Fe_{0.1}MnO₃-TCO ($\Delta = -10.5\%$). It is clear that Fe doping and photoactivation synergistically improve the durability.

4. Conclusion

In conclusion, the La_{1-x}Fe_xMnO₃ ($0 \leq x \leq 0.2$) samples were synthesized successfully via citrate sol-gel method. Under full spectrum illumination of 1.3×10^4 W/m², La_{0.9}Fe_{0.1}MnO₃ exhibited a more superior activity (86.7% toluene conversion and 84.6% CO₂ yield) for toluene oxidation. Through controlled experiments, it was unraveled that the photothermal activity mainly derived from light-driven heat. The results show that the Fe doping and photoactivation synergistically improve the PTCO performance for toluene. Specifically, the doping of Fe not only promotes the formation/regeneration of reactive oxygen species, but improves the mobility and quantity of surface O_{latt}, as well as the low-temperature reducibility; whereas the light supplies the heat energy for the reaction and significantly contributes to the activation of O_{latt} species. Therefore, the co-effect of Fe doping and photoactivation could enhance the PTCO activity, selectivity, resistance to complex gas components, and durability. Moreover, the plausible pathways and mechanisms of toluene oxidation were suggested as adsorbed toluene → benzyl alcohol (in presence of O₂) → benzaldehyde → benzoic acid → maleic anhydride → CO₂ + H₂O. This work opens a new perspective on LaMnO₃-based photothermal catalysts with full spectrum response for VOCs degradation.

CRedit authorship contribution statement

Qi Yu: Conceptualization, Methodology, Data analysis, Investigation, Writing – review & editing. **Caiting Li:** Resources, Supervision, Data curation. **Jungang Zhao:** Methodology, Writing – review & editing, Validation. **Xuan Liu:** Resources, Writing – review & editing, Supervision. **Le Huang:** Writing – review & editing. **Youcai Zhu:** Writing–review & editing. **Kuang Yang:** Writing–review & editing. **Ziang Zhang:** Writing – review & editing. **Dengsheng Ma:** Software, Writing – review & editing. **Ying Zhang:** Visualization, Writing – review & editing. **Qi Huang:** Writing – review & editing.

Declaration of Competing Interest

The authors declare that they have no known competing financial interests or personal relationships that could have appeared to influence the work reported in this paper.

Data Availability

Data will be made available on request.

Acknowledgements

This work was supported by the National Natural Science Foundation of China (52270102), and the Natural Science Foundation of Hunan

Province (2022JJ40071).

Appendix A. Supporting information

Supplementary data associated with this article can be found in the online version at doi:10.1016/j.apcatb.2023.122441.

References

- [1] Y. Liu, J. Deng, S. Xie, Z. Wang, H. Dai, Catalytic removal of volatile organic compounds using ordered porous transition metal oxide and supported noble metal catalysts, *Chin. J. Catal.* 37 (2016) 1193–1205.
- [2] L. Aidaoui, A.G. Triantafyllou, A. Azzi, S.K. Garas, V.N. Matthaïos, Elevated stacks' pollutants' dispersion and its contributions to photochemical smog formation in a heavily industrialized area, *Air Qual. Atmos. Health* 8 (2015) 213–227.
- [3] L. Tan, J. Zhu, X. He, M. Zhou, S. Zhang, The mechanism of toluene absorption by phosphonium ionic liquids with multiple sites, *J. Mol. Liq.* 331 (2021), 115501.
- [4] T. Shou, Y. Li, M.T. Bernards, C. Becco, G. Cao, Y. Shi, Y. He, Degradation of gas-phase o-xylene via combined non-thermal plasma and Fe doped LaMnO₃ catalysts: byproduct control, *J. Hazard. Mater.* 387 (2020), 121750.
- [5] Q. Yu, C. Li, D. Ma, J. Zhao, X. Liu, C. Liang, Y. Zhu, Z. Zhang, K. Yang, Layered double hydroxides-based materials as novel catalysts for gaseous VOCs abatement: Recent advances and mechanisms, *Coord. Chem. Rev.* 471 (2022), 214738.
- [6] F. Wang, J. Deng, S. Impeng, Y. Shen, T. Yan, G. Chen, L. Shi, D. Zhang, Unraveling the effects of the coordination number of Mn over α-MnO₂ catalysts for toluene oxidation, *Chem. Eng. J.* 396 (2020), 125192.
- [7] W. Qu, P. Wang, M. Gao, J.-Y. Hasegawa, Z. Shen, Q. Wang, R. Li, D. Zhang, Delocalization effect promoted the indoor air purification via directly unlocking the ring-opening pathway of toluene, *Environ. Sci. Technol.* 54 (2020) 9693–9701.
- [8] Y. Shen, J. Deng, L. Han, W. Ren, D. Zhang, Low-temperature combustion of toluene over Cu-doped SmMn₂O₅ mullite catalysts via creating highly active Cu²⁺–O–Mn⁴⁺ Sites, *Environ. Sci. Technol.* 56 (2022) 10433–10441.
- [9] Y. Li, S. Wu, J. Wu, Q. Hu, C. Zhou, Photocatalysis for efficient abatement of CO and VOCs, *J. Mater. Chem. A* 8 (2020) 8171–8194.
- [10] Y. Yang, S. Zhao, L. Cui, F. Bi, Y. Zhang, N. Liu, Y. Wang, F. Liu, C. He, X. Zhang, Recent advancement and future challenges of photothermal catalysis for VOCs elimination: From catalyst design to applications, *Green. Energy Environ.* (2022).
- [11] C. Liang, C. Li, Y. Zhu, X. Du, Y. Zeng, Y. Zhou, J. Zhao, S. Li, X. Liu, Q. Yu, Y. Zhai, Light-driven photothermal catalysis for degradation of toluene on CuO/TiO₂ Composite: Dominating photocatalysis and auxiliary thermalcatalysis, *Appl. Surf. Sci.* 601 (2022), 154144.
- [12] R. Ma, J. Sun, D.H. Li, J.J. Wei, Review of synergistic photo-thermo-catalysis: Mechanisms, materials and applications, *Int. J. Hydrog. Energy* 45 (2020) 30288–30324.
- [13] C. Zhou, L. Cheng, Y. Li, M. Zeng, Y. Yang, J. Wu, X. Zhao, Novel photoactivation promotes catalytic abatement of CO on CuO mesoporous nanosheets with full solar spectrum illumination, *Appl. Catal. B-Environ.* 225 (2018) 314–323.
- [14] J. Kong, C. Jiang, Z. Rui, S. Liu, F. Xian, W. Ji, H. Ji, Photothermodynamic synergistic oxidation: an effective way to overcome the negative water effect on supported noble metal catalysts for VOCs oxidation, *Chem. Eng. J.* 397 (2020), 125485.
- [15] J. Kong, Z. Xiang, G. Li, T. An, Introduce oxygen vacancies into CeO₂ catalyst for enhanced coke resistance during photothermodynamic oxidation of typical VOCs, *Appl. Catal. B-Environ.* 269 (2020), 118755.
- [16] J.-J. Li, S.-C. Cai, E.-Q. Yu, B. Weng, X. Chen, J. Chen, H.-P. Jia, Y.-J. Xu, Efficient infrared light promoted degradation of volatile organic compounds over photothermal responsive Pt-rGO-TiO₂ composites, *Appl. Catal. B-Environ.* 233 (2018) 260–271.
- [17] J.-J. Li, E.-Q. Yu, S.-C. Cai, X. Chen, J. Chen, H.-P. Jia, Y.-J. Xu, Noble metal free, CeO₂/LaMnO₃ hybrid achieving efficient photo-thermal catalytic decomposition of volatile organic compounds under IR light, *Appl. Catal. B-Environ.* 240 (2019) 141–152.
- [18] E. Yu, J. Chen, H. Jia, Enhanced light-driven photothermodynamic activity on selectively dissolved LaTi_{1-x}Mn_xO₃+δ perovskites by photoactivation, *J. Hazard. Mater.* 399 (2020), 122942.
- [19] J. Chen, Z. He, G. Li, T. An, H. Shi, Y. Li, Visible-light-enhanced photothermodynamic activity of ABO₃-type perovskites for the decontamination of gaseous styrene, *Appl. Catal. B-Environ.* 209 (2017) 146–154.
- [20] Y. Zheng, W. Wang, D. Jiang, L. Zhang, Amorphous MnO_x modified Co₃O₄ for formaldehyde oxidation: improved low-temperature catalytic and photothermodynamic activity, *Chem. Eng. J.* 284 (2016) 21–27.
- [21] P. Kanhere, Z. Chen, A review on visible light active perovskite-based photocatalysts, *Molecules* (2014) 19995–20022.
- [22] W. Si, Y. Wang, Y. Peng, J. Li, Selective dissolution of A-site cations in ABO₃ perovskites: a new path to high-performance catalysts, *Angew. Chem. Int. Ed.* 54 (2015) 7954–7957.
- [23] W. Yang, R. Zhang, B. Chen, N. Bion, D. Duprez, S. Royer, Activity of perovskite-type mixed oxides for the low-temperature CO oxidation: evidence of oxygen species participation from the solid, *J. Catal.* 295 (2012) 45–58.
- [24] Y. Xu, J. Dhainaut, J.-P. Dacquin, A.-S. Mamede, M. Marinova, J.-F. Lamonier, H. Vezin, H. Zhang, S. Royer, La_{1-x}(Sr, Na, K)_xMnO₃ perovskites for HCHO oxidation: the role of oxygen species on the catalytic mechanism, *Appl. Catal. B Environ.* 287 (2021), 119955.

- [25] L. Zhao, L. Jiang, Y. Huang, J. Zhang, J. Tang, C. Li, Mechanism investigation of three-dimensional porous A-site substituted $\text{La}_{1-x}\text{Co}_x\text{FeO}_3$ catalysts for simultaneous oxidation of NO and toluene with H_2O , *Appl. Surf. Sci.* 578 (2022), 151977.
- [26] M. Wang, T. Zhao, X. Dong, M. Li, H. Wang, Effects of Ce substitution at the A-site of $\text{LaNi}_{0.5}\text{Fe}_{0.5}\text{O}_3$ perovskite on the enhanced catalytic activity for dry reforming of methane, *Appl. Catal. B-Environ.* 224 (2018) 214–221.
- [27] Y. Wang, Y. Zheng, Y. Wang, H. Wang, X. Zhu, Y. Wei, Y. Wang, L. Jiang, Z. Yang, K. Li, Evaluation of Fe substitution in perovskite LaMnO_3 for the production of high purity syngas and hydrogen, *J. Power Sources* 449 (2020), 227505.
- [28] B. Song, C. Li, X. Du, S. Li, Y. Zhang, Y. Lyu, Q. Zhou, Superior performance of Cu-Ce binary oxides for toluene catalytic oxidation: Cu-Ce synergistic effect and reaction pathways, *Fuel* 306 (2021), 121654.
- [29] E. Yu, J. Li, J. Chen, J. Chen, Z. Hong, H. Jia, Enhanced photothermal catalytic degradation of toluene by loading Pt nanoparticles on manganese oxide: Photoactivation of lattice oxygen, *J. Hazard. Mater.* 388 (2020), 121800.
- [30] J. Chen, X. Chen, W. Xu, Z. Xu, J. Chen, H. Jia, J. Chen, Hydrolysis driving redox reaction to synthesize Mn-Fe binary oxides as highly active catalysts for the removal of toluene, *Chem. Eng. J.* 330 (2017) 281–293.
- [31] C. Zhang, Y. Guo, Y. Guo, G. Lu, A. Boreave, L. Retaileau, A. Baylet, A. Giroir-Fendler, LaMnO_3 perovskite oxides prepared by different methods for catalytic oxidation of toluene, *Appl. Catal. B-Environ.* 148–149 (2014) 490–498.
- [32] N.E. Machin, C. Karakaya, A. Celepci, Catalytic combustion of methane on La-, Ce-, and Co-based mixed oxides, *Energy Fuel* 22 (2008) 2166–2171.
- [33] C. Zhang, C. Wang, W. Zhan, Y. Guo, Y. Guo, G. Lu, A. Baylet, A. Giroir-Fendler, Catalytic oxidation of vinyl chloride emission over LaMnO_3 and $\text{La}_{0.2}\text{Mn}_{0.8}\text{O}_3$ (B_{12}Co , Ni, Fe) catalysts, *Appl. Catal. B Environ.* 129 (2013) 509–516.
- [34] X. Zhao, Q. Yang, J. Cui, XPS study of surface absorbed oxygen of ABO₃ mixed oxides, *J. Rare Earth* 26 (2008) 511–514.
- [35] W. Tang, X. Wu, D. Li, Z. Wang, G. Liu, H. Liu, Y. Chen, Oxalate route for promoting activity of manganese oxide catalysts in total VOCs' oxidation: effect of calcination temperature and preparation method, *J. Mater. Chem. A* 2 (2014) 2544–2554.
- [36] M. Romero-Sáez, D. Divakar, A. Aranzabal, J.R. González-Velasco, J.A. González-Marcos, Catalytic oxidation of trichloroethylene over Fe-ZSM-5: Influence of the preparation method on the iron species and the catalytic behavior, *Appl. Catal. B-Environ.* 180 (2016) 210–218.
- [37] C. Ge, Y. Yu, D. An, Q. Tong, C. Tang, F. Gao, J. Sun, L. Dong, Surface configuration modulation for FeOx-CeO₂/γ-Al₂O₃ catalysts and its influence in CO oxidation, *J. Catal.* 386 (2020) 139–150.
- [38] Y. Wang, J. Wu, G. Wang, D. Yang, T. Ishihara, L. Guo, Oxygen vacancy engineering in Fe doped akhtenskite-type MnO_2 for low-temperature toluene oxidation, *Appl. Catal. B-Environ.* 285 (2021), 119873.
- [39] X. Liu, J. Mi, L. Shi, H. Liu, J. Liu, Y. Ding, J. Shi, M. He, Z. Wang, S. Xiong, Q. Zhang, Y. Liu, Z.-S. Wu, J. Chen, J. Li, In situ modulation of a-site vacancies in $\text{LaMnO}_{3.15}$ perovskite for surface lattice oxygen activation and boosted redox reactions, *Angew. Chem. Int. Ed.* 60 (2021) 26747–26754.
- [40] Y.P. Wang, L. Zhou, M.F. Zhang, X.Y. Chen, J.M. Liu, Z.G. Liu, Room-temperature saturated ferroelectric polarization in BiFeO₃ ceramics synthesized by rapid liquid phase sintering, *Appl. Phys. Lett.* 84 (2004) 1731–1733.
- [41] L. Liu, J. Sun, J. Ding, Y. Zhang, T. Sun, J. Jia, Highly active $\text{Mn}_{3-x}\text{Fe}_x\text{O}_4$ spinel with defects for toluene mineralization: insights into regulation of the oxygen vacancy and active metals, *Inorg. Chem.* 58 (2019) 13241–13249.
- [42] S. Mo, Q. Zhang, J. Li, Y. Sun, Q. Ren, S. Zou, Q. Zhang, J. Lu, M. Fu, D. Mo, J. Wu, H. Huang, D. Ye, Highly efficient mesoporous MnO_2 catalysts for the total toluene oxidation: Oxygen-Vacancy defect engineering and involved intermediates using in situ DRIFTS, *Appl. Catal. B-Environ.* 264 (2020), 118464.
- [43] H. Sun, Z. Liu, S. Chen, X. Quan, The role of lattice oxygen on the activity and selectivity of the OMS-2 catalyst for the total oxidation of toluene, *Chem. Eng. J.* 270 (2015) 58–65.
- [44] Y. Liu, H. Dai, J. Deng, Y. Du, X. Li, Z. Zhao, Y. Wang, B. Gao, H. Yang, G. Guo, In situ poly(methyl methacrylate)-templating generation and excellent catalytic performance of $\text{MnO}_x/3\text{DOM LaMnO}_3$ for the combustion of toluene and methanol, *Appl. Catal. B-Environ.* 140–141 (2013) 493–505.
- [45] L. Liu, J. Li, H. Zhang, L. Li, P. Zhou, X. Meng, M. Guo, J. Jia, T. Sun, In situ fabrication of highly active γ- $\text{MnO}_2/\text{SmMnO}_3$ catalyst for deep catalytic oxidation of gaseous benzene, ethylbenzene, toluene, and o-xylene, *J. Hazard. Mater.* 362 (2019) 178–186.
- [46] X. Lin, S. Li, H. He, Z. Wu, J. Wu, L. Chen, D. Ye, M. Fu, Evolution of oxygen vacancies in $\text{MnO}_x\text{-CeO}_2$ mixed oxides for soot oxidation, *Appl. Catal. B-Environ.* 223 (2018) 91–102.
- [47] Y. Feng, C. Wang, C. Wang, H. Huang, H.-C. Hsi, E. Duan, Y. Liu, G. Guo, H. Dai, J. Deng, Catalytic stability enhancement for pollutant removal via balancing lattice oxygen mobility and VOCs adsorption, *J. Hazard. Mater.* 424 (2022), 127337.
- [48] M. Zeng, Y. Li, M. Mao, J. Bai, L. Ren, X. Zhao, Synergetic effect between photocatalysis on TiO_2 and thermocatalysis on CeO_2 for gas-phase oxidation of benzene on $\text{TiO}_2/\text{CeO}_2$ nanocomposites, *ACS Catal.* 5 (2015) 3278–3286.
- [49] Y.-K. Hsu, Y.-C. Chen, Y.-G. Lin, L.-C. Chen, K.-H. Chen, Birnessite-type manganese oxides nanosheets with hole acceptor assisted photoelectrochemical activity in response to visible light, *J. Mater. Chem.* 22 (2012) 2733–2739.
- [50] Y. Yang, Y. Li, M. Mao, M. Zeng, X. Zhao, UV-visible-infrared light driven thermocatalysis for environmental purification on ramsdellite MnO_2 hollow spheres considerably promoted by a novel photoactivation, *ACS Appl. Mater. Inter.* 9 (2017) 2350–2357.
- [51] G. Gao, Y. Liao, W. Li, Z. Li, H. Xu, W. Huang, N. Yan, L. Fan, Z. Qu, Active surface RuO_x species originating from size-driving self-dispersion process for toluene catalytic combustion, *Chem. Eng. J.* 441 (2022), 136127.
- [52] Z. Su, W. Yang, C. Wang, S. Xiong, X. Cao, Y. Peng, W. Si, Y. Weng, M. Xue, J. Li, Roles of oxygen vacancies in the bulk and surface of CeO_2 for toluene catalytic combustion, *Environ. Sci. Technol.* 54 (2020) 12684–12692.
- [53] Y. Zhang, A. Martin, H. Berndt, B. Lücke, M. Meisel, FTIR investigation of surface intermediates formed during the ammoxidation of toluene over vanadyl pyrophosphate, *J. Mol. Catal. A: Chem.* 118 (1997) 205–214.
- [54] Z. Chen, Y. Peng, J. Chen, C. Wang, H. Yin, H. Wang, C. You, J. Li, Performance and mechanism of photocatalytic toluene degradation and catalyst regeneration by thermal/UV treatment, *Environ. Sci. Technol.* 54 (2020) 14465–14473.
- [55] J. Zhong, Y. Zeng, D. Chen, S. Mo, M. Zhang, M. Fu, J. Wu, Z. Su, P. Chen, D. Ye, Toluene oxidation over Co³⁺-rich spinel Co_3O_4 : evaluation of chemical and by-product species identified by in situ DRIFTS combined with PTR-TOF-MS, *J. Hazard. Mater.* 386 (2020), 121957.
- [56] Y. Shen, J. Deng, S. Impeng, S. Li, T. Yan, J. Zhang, L. Shi, D. Zhang, Boosting toluene combustion by engineering Co-O strength in cobalt oxide catalysts, *Environ. Sci. Technol.* 54 (2020) 10342–10350.
- [57] K. Li, J. Chen, B. Bai, S. Zhao, F. Hu, J. Li, Bridging the reaction route of toluene total oxidation and the structure of ordered mesoporous Co_3O_4 : the roles of surface sodium and adsorbed oxygen, *Catal. Today* 297 (2017) 173–181.
- [58] J. He, L. Chen, D. Ding, Y.-K. Yang, C.-T. Au, S.-F. Yin, Facile fabrication of novel $\text{Cd}_3(\text{C}_3\text{N}_3\text{S}_3)_2/\text{CdS}$ porous composites and their photocatalytic performance for toluene selective oxidation under visible light irradiation, *Appl. Catal. B-Environ.* 233 (2018) 243–249.
- [59] F. Arena, G. Trunfio, J. Negro, B. Fazio, L. Spadaro, Basic evidence of the molecular dispersion of MnCeO_x catalysts synthesized via a novel “redox-precipitation” route, *Chem. Mater.* 19 (2007) 2269–2276.
- [60] A.R. Gandhe, J.S. Rebello, J.L. Figueiredo, J.B. Fernandes, Manganese oxide OMS-2 as an effective catalyst for total oxidation of ethyl acetate, *Appl. Catal. B-Environ.* 72 (2007) 129–135.
- [61] Z. Wang, S. Xie, Y. Feng, P. Ma, K. Zheng, E. Duan, Y. Liu, H. Dai, J. Deng, Simulated solar light driven photothermal catalytic purification of toluene over iron oxide supported single atom Pt catalyst, *Appl. Catal. B-Environ.* 298 (2021), 120612.
- [62] X. Du, C. Li, L. Zhao, J. Zhang, L. Gao, J. Sheng, Y. Yi, J. Chen, G. Zeng, Promotional removal of HCHO from simulated flue gas over Mn-Fe oxides modified activated coke, *Appl. Catal. B-Environ.* 232 (2018) 37–48.